Compact and Efficient Bipolar Coupler for Wireless Power Chargers: Design and Analysis

Junjun Deng, *Member, IEEE*, Weihan Li, *Student Member, IEEE*, Trong Duy Nguyen, Siqi Li, *Member, IEEE*, and Chunting Chris Mi, *Fellow, IEEE*

***Abstract*—Compactness and efficiency are the two basic considerations of the wireless battery chargers for electric vehicles (EVs) and plug-in hybrid EVs. The double-sided LCC compensation topology for wireless power transfer (WPT) has been proved to be one of the efficient solutions lately. However, with the increase of the numbers of compensation components, the volume of the system may become larger, which makes it less attractive. To improve the compactness, a bipolar coupler structure with a compensation-integrated feature is proposed. The inductors of the LCC compensation networks are designed as planar-type and attached to the power-transferring main coils. Extra space and magnetic cores for the compensated inductors outside of the coupler are saved. The cost is that extra couplings between the compensated coils (inductors) and the main coils are induced. To validate the feasibility, the proposed coupler is modeled and investigated by 3-D finite-element analysis tool first. The positioning of the compensated coils, the range of the extra couplings, and the tolerance to misalignment are studied. This is followed by the circuit modeling and characteristic analysis of the proposed WPT topology based on the fundamental harmonic approximation. At last, a 600 mm $\times$ 600 mm with a nominal 150-mm-gap wireless charger prototype, operated at a resonant frequency of 95 kHz and a rated power of 5.6 kW has been built and tested. A peak efficiency of 95.36% from a dc power source to the battery load is achieved at rated operation condition.**

***Index Terms*—Electric vehicle (EV), inductive power transfer (IPT), magnetically coupled system, magnetic integrated compensation, stationary charging, wireless charger, wireless power transfer (WPT).**

Manuscript received November 2, 2014; revised January 19, 2015; accepted March 17, 2015. Date of publication March 30, 2015; date of current version July 10, 2015. This work was supported in part by the U.S. Department of Energy Graduate Automotive Technology Education Grant; the U.S.–China Clean Energy Research Center—Clean Vehicle Consortium, DENSO International, the University of Michigan and China Scholarship Council. Recommended for publication by Associate Editor Y. J. Jang.

J. Deng is with the School of Automation, Northwestern Polytechnical University, Xi'an, 710072 China, and also with the Department of Electrical and Computer Engineering, University of Michigan, Dearborn, MI 48128 USA (e-mail: dengjunjun1985@gmail.com).

W. Li is with the Department of Electrical and Computer Engineering, University of Michigan, Dearborn, MI 48128 USA, and also with the School of Mechanical and Automotive Engineering, Hefei University of Technology, Hefei 230009, China (e-mail: weihanli1988@gmail.com).

T. D. Nguyen is with DENSO International America, Inc., Southfield, MI 48033 USA (e-mail: ntrduy@gmail.com).

S. Li is with the Electrical Engineering Department, Kunming University of Science and Technology, Kunming 650500, China (e-mail: lisiqi00@gmail.com).

C. C. Mi is with the Department of Electrical and Computer Engineering, University of Michigan, Dearborn, MI 48128 USA (e-mail: chrismi@umich.edu).

Color versions of one or more of the figures in this paper are available online at http://ieeexplore.ieee.org.

Digital Object Identifier 10.1109/TPEL.2015.2417115

I. Introduction

OVER the last decade, the demand for plug-in hybrid electric vehicles (PHEVs) and pure electric vehicles (EVs) has been growing because of the increase in greenhouse-gas emissions and the fossil-fuel price fluctuations [1]. However, the range anxiety, high cost, and inconvenience of charging are still the major barriers to the overall acceptance of PHEVs and EVs [2]. The wireless power transfer (WPT) technology has been regarded as a potential solution to remove the third barrier since an efficient wireless charger can significantly improve the ease of charging for the end users [3], [4]. Thus, there has been a growing interest in applying WPT technology to develop practical wireless charging systems. Several aspects of WPT have been studied, such as magnetic coupler design techniques, compensation topologies, control methods, foreign object detection algorithms, and the radiation safety issues [5]. Among them, the researchers have been dominantly focused on magnetic coupler design and compensation circuits in the past decade.

The magnetic couplers of WPT chargers are loosely coupled transformers in which the primary and secondary coils are linked across a relatively large air gap. In a stationary charging system, the coupler is usually designed as a pad form. The coupling coefficient k is greatly affected by the design of the coupler. It is preferred to have higher k and tolerance to misalignment with the minimum dimension and cost. Different kinds of coupler geometry and configuration have been proposed to reach the goal. Circular coupler designs have been well researched and optimized [6]–[8]. The 700-mm-diameter circular pad in [6] had a coupling coefficient of 0.2, with a 175-mm air gap. However, the diameter of a circular pad needs to be increased significantly in order to achieve good coupling with a larger air gap. A flux-pipe coupler was introduced as an attempt to improve coupling [9], [10]. Although its ability of throwing flux to a pickup pad is approximately doubled compared to the circular topology, it suffers from a significant drop in efficiency when aluminum is used to shield the flux behind the pads to prevent the eddy current loss in the EV chassis. Because the flux pipe produces a doubled-sided flux path, the nonuseful flux coming out of the back of the pad is equal to the useful flux coming out of the front. To combine the advantages of both the circular and flux-pipe designs, a bipolar single-sided flux coupler, which is also named DD pad, is proposed [11]. The flux path height and the effective charge zone of a DD pad could be two times larger than a circular pad with similar material cost. The DD pads have a better tolerance in the x-direction than that in the y-direction as shown in Fig. 1. Besides, there is a null point in the y-direction at about 34% misalignment [11]. In practice,

0885-8993 © 2015 IEEE. Personal use is permitted, but republication/redistribution requires IEEE permission.
See http://www.ieee.org/publications_standards/publications/rights/index.html for more information.

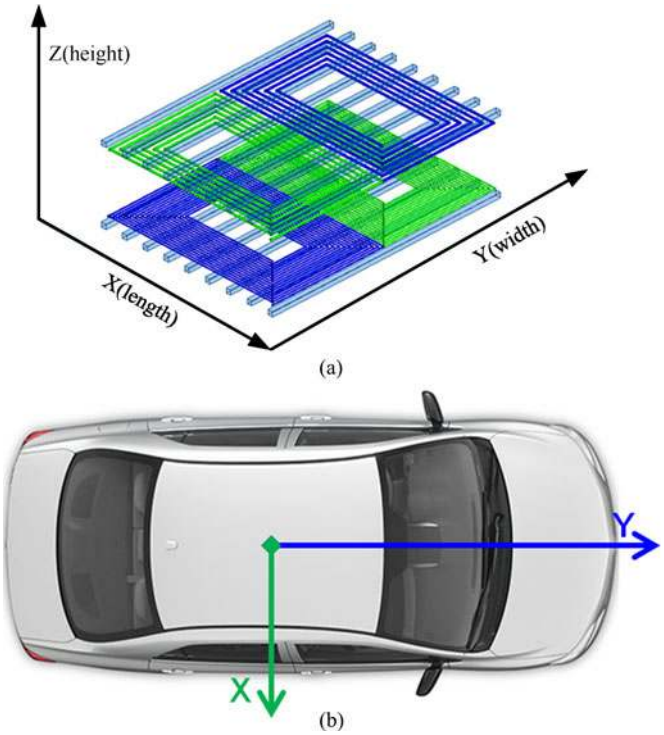

Fig. 1. (a) DD bipolar pads. (b) Typical misalignments in EV: *x*-axis: door-to-door misalignment, *y*-axis: front-to-rear misalignment.

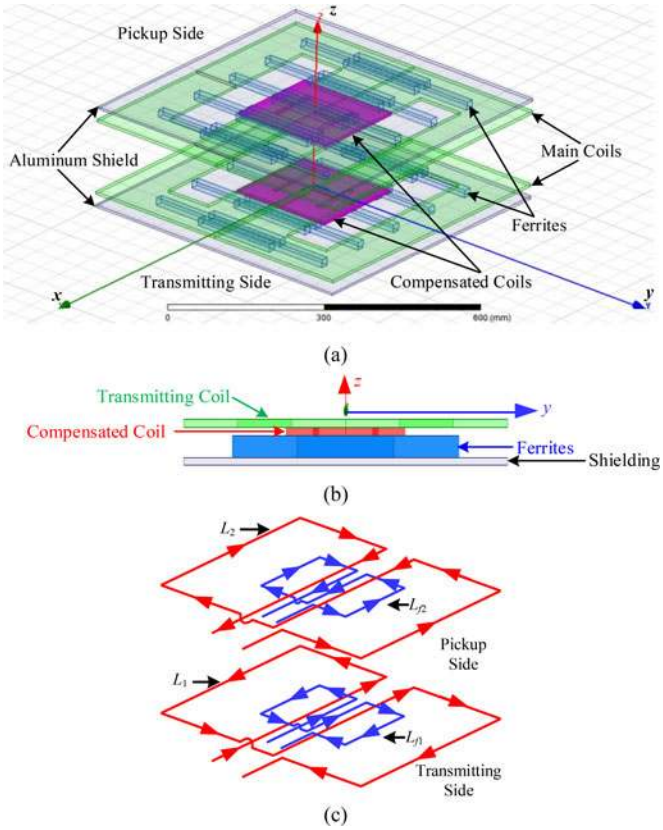

Fig. 2. Proposed structure of WPT DD pads with integrated compensation inductors. (a) Three-dimensional model of the pads. (b) Side view of the transmitting pad. (c) Simplified coils and the current reference direction.

a symmetrical tolerance ability is not always necessary. There are mainly two types of misalignment that raise the concern in the EV charging application: door-to-door and front-to-rear, as illustrated in Fig. 1(b). The first is more crucial because once an EV is being parked, it is inconvenient to adjust the door-to-door misalignment, while the latter is much easier for the driver to adjust with the help of a simple visual feedback. Hence, the DD pad configuration could be suitable. In this case, the better misalignment tolerance of a DD pad should be chosen for the door-to-door misalignment, while the worse one can be chosen for the front-to-rear misalignment.

On the other side, compensation circuits are usually used to construct resonant tanks between the converters and the coils for minimizing the power supply VA rating and increasing power-transfer capability [12], [13]. Different compensation topologies have been proposed and implemented in a wide range of applications. Depending on the way that the compensation capacitors are connected with the transmitting and pickup coils, four basic topologies named series–series (SS), series–parallel (SP), parallel–series (PS), and parallel–parallel (PP) are widely adopted [14], [15]. The SS and SP topologies were more commonly seen, because in voltage-fed resonant converter power supplies, the resonant networks require series tuning at the input port, and are more readily accessible. For SP compensation, the circuit is easily mistuned since the primary compensated capacitance relates to the coupling. In comparison, the compensation capacitance can be a constant value for fully compensated SS method regardless of the coupling and load variation. However, it has poor output voltage regulation capability [16]. The partially compensated SS method improves the characteristic of the load regulation. But the parameter design becomes tricky for control stability and soft-switching realization. For better performance, SP LC compensation [17], and SP LCC [18] compensation are proposed. By inducing an LCC compensation network on the primary side, part of the transmitting coil inductance is compensated by the series-connected capacitor. In addition, an LCL-T voltage-fed resonant converter can be formed. When the converter operates at the resonant frequency, it performs like a constant current (CC) source [19]. The sinusoidal current injected to the primary coil only depends on the converter input voltage, regardless the load and coupling variation, which greatly simplifies the primary control complexity. Meanwhile, by applying the same LCC compensation network on the secondary side, a unit power factor pickup can be realized. This topology improves the efficiency by minimizing the circulating current through the pickup coil and the reflected reactive loading on the primary side [20].

From the above, a potential solution for the efficient EV wireless charger application can be found: well-designed DD pads with LCC compensation networks applying to both the primary and the secondary side [21]. However, the increased amount in the usage of passive elements to construct the LCC network makes the whole system bulky. Although the compensation capacitors can be either embedded in the pads or placed in the printed circuit boards of the power supply. The positioning of the compensated inductors is more difficult to handle.

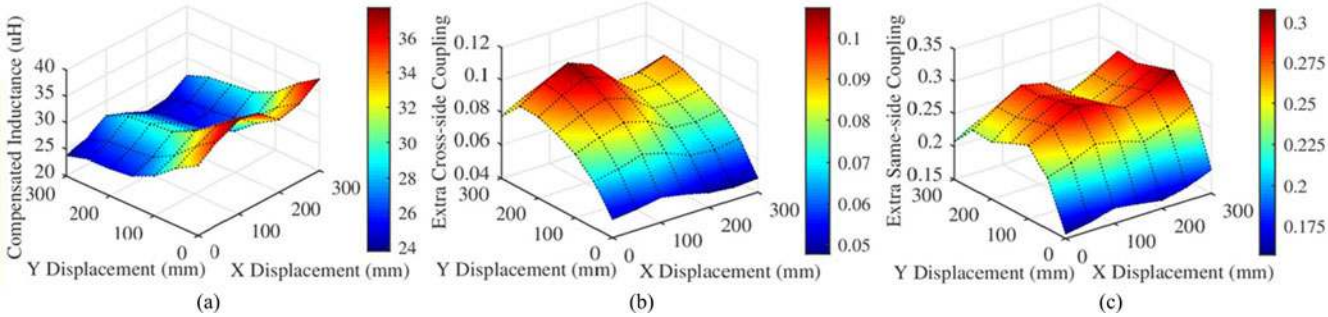

Fig. 3. Impact of the positioning of the compensated coil: (a) Inductance variation with different primary compensated coil placement. (b) Coupling variation between the primary main coil and the secondary compensated coil. (c) Coupling variation between the primary main coil and the primary compensated coil.

Additional magnetic cores and heat-dissipation considerations are required since the currents through the compensated inductors are in the same level as the coupled coils. The focus of this paper is to mitigate these drawbacks in applying double-sided LCC compensation for EV wireless chargers. Inspired by the approach in which the impedance matching network is inductively coupled with the resonators in the mid-range applications [22], a novel coupler structure that features the magnetic integration is proposed. The inductors of the LCC compensation circuits are designed to be planar-DD-type and inserted into the DD pads to share the cores. The configuration of the proposed coupler structure is introduced and investigated by finite-element analysis (FEA) in Section II. Subsequently, the circuit model of the integrated topology is outlined. The impact of the extra integration-induced couplings between the compensated coils and the main coils (transmitting coil and pickup coil) is analyzed thoroughly in Section III. This is followed by the experimental verification and final conclusions in Section IV and Section V, respectively.

II. Proposed Magnetic Coupler Structure

The proposed WPT compensation-integrated DD pad structure is shown in Fig. 2. The transmitting pad and the pickup pad are identical. Each pad is composed of four layers. Taking the transmitting pad shown in Fig. 2(b) as an example, the power-transferring coil (main coil) is placed on the top layer. As a distinguishing feature, another coil with a smaller size lies below the main coil. The coil in the second layer serves as the compensated inductor of the LCC network. Further down, a ferrite layer is inserted for coupling enhancement and flux guidance. At the bottom, a thin aluminum sheet is used for the shielding. By inserting an additional coil between the main coil and the ferrites, the compensated inductor is integrated magnetically and spatially.

The original intention of the proposed structure was to gather the magnetic components of the same side together to share the cores. However, in this case, all the main coils and compensated coils are inevitably coupled with each other due to the pads' loosely coupled nature. Therefore, some basic design considerations of the compensated coils should be explored. First of all, the same DD shape used for the main coils is chosen intuitively for the compensated coils considering that the ferrite arrangement works better for bipolar coils. Second, because the fundamental flux path height of the DD coil is about half of its length [11], the size of the compensated coils should be less than twice of the pads' nominal vertical clearance to be decoupled. Third, in order to find out the impact of the positioning of the compensated coils, a 3-D FEA tool is utilized to model the proposed structure. A magnetic coupler with the main coil sized at 600 mm $\times$ 600 mm and vertical gap of 150 mm is modeled. The compensated coil size is chosen to be 200 mm $\times$ 200 mm accordingly. The simulation results are shown in Fig. 3. It is to be noted that the coordinates in Fig. 3 are defined as indicated in Fig. 2(a). The study is focused on the compensated inductance, the extra cross-side couplings, and the extra same-side couplings. The extra cross-side couplings are defined as the couplings between the main coils and compensated coils distributed on different sides, while the extra same-side couplings indicate the coupled coils are coming from the same side. As shown in Fig. 3(a), it is easier to obtain a larger inductance when the compensated coils are placed along the *x*-axis. Moreover, both the extra cross-side couplings and the extra same-side couplings tend to be smaller along the *x*-axis as in Fig. 3(b) and 3(c). However, the extra cross-side couplings are reduced when the compensated coils move toward the edge along the *x*-axis, whereas the same-side couplings are increased under the same condition. Hence, the compensated coils can be placed at the center of the pad to have higher inductance and smaller extra couplings overall.

On the other hand, the variations of the couplings and variations of the inductances are very important to the circuit modeling. In accordance with the inductor designators shown in Fig. 2(c), the coupling coefficients are defined as

$$\begin{aligned} k &= M / \sqrt{L_1 L_2}, \\ k_{11} &= M_{11} / \sqrt{L_1 L_{f1}} = M_{22} / \sqrt{L_2 L_{f2}} = k_{22}, \\ k_{12} &= M_{1f2} / \sqrt{L_1 L_{f2}} = M_{2f1} / \sqrt{L_2 L_{f1}} = k_{21}, \\ k_{f1f2} &= M_{f1f2} / \sqrt{L_{f1} L_{f2}} \end{aligned} \tag{1}$$

where L_1 and L_2 are the self-inductances of the transmitting coil and pickup coil, respectively, and M is the mutual inductance between them. L_{f1}, L_{f2}, and M_{f1f2} are the self-inductances and mutual inductance of the compensated coils. M_{1f2} denotes the extra cross-side mutual inductance between L_1, L_{f2}, and so on. The misaligned situations along the *x*-axis and *y*-axis are

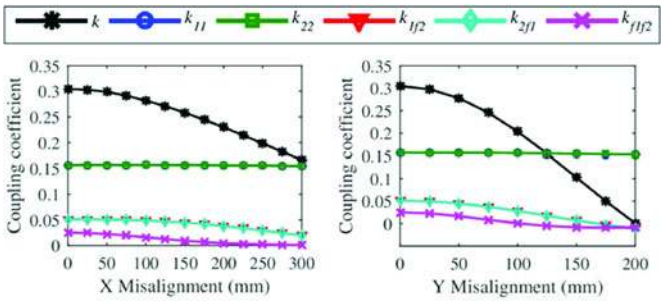

Fig. 4. Coupling variation with horizontal misalignments.

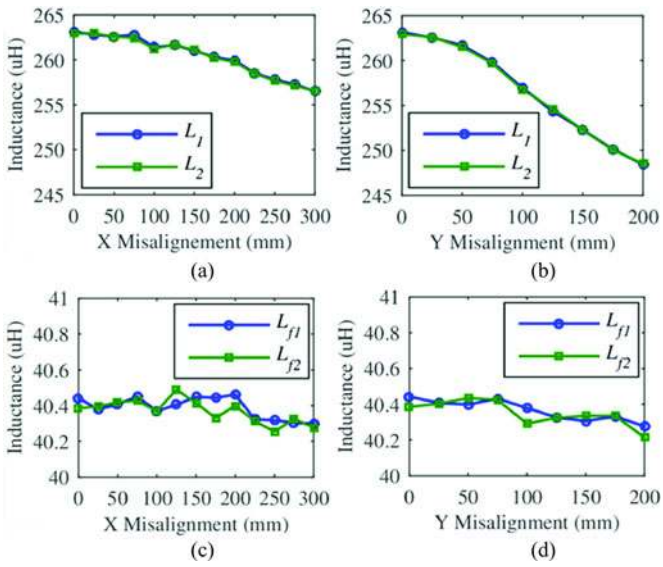

Fig. 5. Inductance variations with horizontal misalignments. (a) Inductances of the main coils. (b) Inductances of the compensated coils.

swept, respectively, in the FEA tool. The simulation results are shown in Figs. 4 and 5. As shown in Fig. 4, the main coupling k drops faster along the y-direction. If the lower limit of k is set as 0.15, the x-direction and y-direction misalignment tolerance could be ± 300 and ± 125 mm, respectively. Second, because the coils distributed in the same side are attached together. The extra same-side couplings k_{11} and k_{22} can be regarded as constants regardless of misalignment, which Fig. 4 confirms. In addition, the extra cross-side couplings, k_{12} and k_{21}, are quite small and continue to shrink when the misalignment happens. The coupling between the compensated coils (k_{f1f2}) is even smaller, which is only one half of the extra cross-side couplings. Given that the self-inductances of the compensated coils are several times smaller than the main coils' self-inductances, the mutual inductance between the compensated coils M_{f1f2} is negligible, while the extra cross-side mutual inductances M_{1f2} and M_{2f1} should be considered at the designed frequency. Furthermore, in Fig. 5(a), it can be observed that the main coil inductance is slightly affected by the misalignments. The variation in x-misaligned condition (2%) is smaller than that seen in y-misaligned condition (5%). The results in Fig. 5(b) show that the compensated inductance remains constant, since the additional coils are attached to the ferrites tightly.

III. Analysis of the Proposed Topology

A. Circuit Modeling

Based on the FEA results presented in Section II, the circuit diagram of the proposed double-sided LCC compensated WPT system with a magnetic integration feature can be drawn as Fig. 6. A voltage-fed full-bridge converter is formed by MOSFETs S_1–S_4. L_{f1}, C_{f1}, and C_1 are the primary-side compensation inductor and capacitors, while L_{f2}, C_{f2}, and C_2 form the pickup side compensation network. As mentioned previously, the mutual inductance between L_{f1} and L_{f2} can be dismissed, so there are five couplings that should be taken into account. The extra same-side couplings and the compensated inductance are constants as simulated. In addition, the extra cross-side couplings become smaller when the misalignment happens. However, considering that the maximum value of k_{12} and k_{21} is relatively small, the variation of the corresponding mutual inductances due to misalignments is acceptable to be neglected.

To focus on the feasibility analysis, the slight fluctuations of the main coils' self-inductances and all the parasitic parameters of the components are neglected in the following discussion. Besides, the fundamental harmonic approximation is applied under static-state conditions. The effects of the extra same-side couplings can be analyzed by the decoupled equivalent circuit, since common ports can be easily found. Fig. 7 uses the primary side as an example to provide the equivalent circuits of the inductor-coupled primary resonant tank. First, the coupled primary inductors L_{f1} and L_1, shown in Fig. 7(a), can be decoupled by inducing the mutual inductors as shown in Fig. 7(b). Then, the mutual inductors can be lumped together as part of the compensated LCC network. As shown in Fig. 7(c), the equivalent compensation circuit parameters can be written as

$$\begin{aligned} L_{f1e} &= L_{f1} + M_{11}, \\ C_{f1e} &= \frac{C_{f1}}{\omega^2 M_{11} \cdot C_{f1} + 1}, \\ C_{1e} &= \frac{C_1}{1 - \omega^2 M_{11} \cdot C_1} \end{aligned} \tag{2}$$

where ω is the operating angular frequency. As mentioned earlier, the purpose of incorporating the LCC compensation network in WPT is to form the LCL-T resonant converter. To achieve this, the reactance of each branch X_1 is tuned by the equations in [3], [19]

$$X_1 = \omega_0 L_{f1e} = \frac{1}{\omega_0 C_{f1e}} = \omega_0 L_{1e} = \omega_0 \left(L_1 - \frac{1}{\omega_0^2 C_{1e}} \right) \tag{3}$$

where ω_0 is the resonant frequency defined by

$$\omega_0 = \frac{1}{\sqrt{L_{f1e} C_{f1e}}} = \frac{1}{\sqrt{L_{f1} C_{f1}}}. \tag{4}$$

From (3) and (4), we can derive

$$\frac{1}{\omega_0^2 C_1} = L_{1e} - L_{f1e} = L_1 - L_{f1}. \tag{5}$$

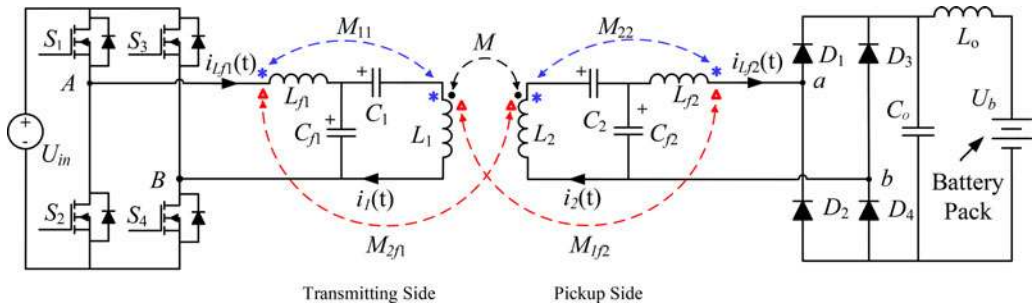

Fig. 6. Magnetic-integrated double-sided *LCC* compensation topology for WPT.

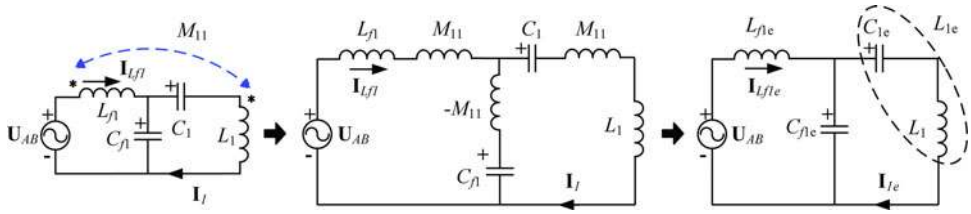

Fig. 7. Primary compensation network considered the coupling between the same-side inductors. (a) Actual circuit. (b) Decoupled circuit. (c) Equivalent circuit.

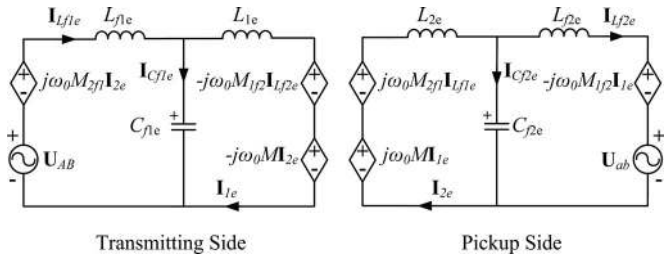

Fig. 8. Equivalent circuit of the proposed magnetic-integrated WPT topology.

It can be seen that the resonant frequency and the series-compensated capacitors maintain the same value regardless of magnetic integration. The same applies to the receiving side compensation network.

To analyze the couplings that involve coils distributed on different sides, which include the main coupling (k) and the extra cross-side couplings (k_{12} and k_{21}), the coupled inductors can be modeled with the use of dependent voltage sources. Fig. 8 shows an equivalent circuit of the proposed WPT topology. It can be seen below that the transmitting and pickup circuits are symmetrically identical. Each LCL-T compensation network is tuned to the primary resonant frequency defined by (4). By Kirchhoff's Laws, it is easy to attain

$$\begin{aligned}
\mathbf{I}_{1e} &= \frac{\mathbf{U}_{AB}}{j\omega_0 L_{f1e}} + \frac{M_{2f1}}{L_{f1e}}\mathbf{I}_{2e} \\
\mathbf{I}_{Lf1e} &= \frac{M}{L_{f1e}}\mathbf{I}_{2e} + \frac{M_{1f2}}{L_{f1e}}\mathbf{I}_{Lf2e} \\
\mathbf{I}_{2e} &= -\frac{\mathbf{U}_{ab}}{j\omega_0 L_{f2e}} + \frac{M_{1f2}}{L_{f2e}}\mathbf{I}_{1e} \\
\mathbf{I}_{Lf2e} &= \frac{M}{L_{f2e}}\mathbf{I}_{1e} + \frac{M_{2f1}}{L_{f2e}}\mathbf{I}_{Lf1e}
\end{aligned} \tag{6}$$

where $\mathbf{U}_{AB}$ is the voltage phasor applied on the primary side, $\mathbf{I}_{Lf1e}$ is the current phasor through the primary inductor L_{f1e}, $\mathbf{I}_{Lf_{2e}}$ is the current phasor through the secondary inductor L_{f2e}, $\mathbf{I}_{1e}$ is the current phasor through the transmitting coil, $\mathbf{I}_{2e}$ is the current phasor through the pickup coil, and $\mathbf{U}_{ab}$ is the voltage phasor applied at the secondary rectifier.

At a given input voltage and output battery voltage, the current phasors can be solved

$$\begin{aligned}
\mathbf{I}_{Lf1e} &= j\Delta_1\mathbf{U}_{ab} - j\Delta_2\mathbf{U}_{AB} \\
\mathbf{I}_{Lf2e} &= -j\Delta_1\mathbf{U}_{AB} + j\Delta_2\mathbf{U}_{ab} \\
\mathbf{I}_{1e} &= -j\frac{L_{f2e}}{\omega_0 \mathrm{X}_i}\mathbf{U}_{AB} + j\frac{M_{2f1}}{\omega_0 \mathrm{X}_i}\mathbf{U}_{ab} \\
\mathbf{I}_{2e} &= j\frac{L_{f1e}}{\omega_0 \mathrm{X}_i}\mathbf{U}_{ab} - j\frac{M_{1f2}}{\omega_0 \mathrm{X}_i}\mathbf{U}_{AB}
\end{aligned} \tag{7}$$

where

$$\begin{aligned}
\Delta_1 &= M\left(L_{f1e}L_{f2e} + M_{1f2}M_{2f1}\right) / \left(\omega_0 \mathrm{X}_i^2\right) \\
\Delta_2 &= 2zML_{f2e}M_{1f2} / \left(\omega_0 \mathrm{X}_i^2\right) \\
\mathrm{X}_i &= L_{f1e}L_{f2e} - M_{1f2}M_{2f1}.
\end{aligned} \tag{8}$$

For comparison, the behaviors of the nonintegrated double-sided LCC compensated WPT system can be described by forcing the extra couplings to be zero ($M_{1f2} = M_{2f1} = 0$) and taking $\mathbf{U}_{AB}$ as the reference ($\mathbf{U}_{AB} = U_{AB}\angle 0°$)

$$\begin{aligned}
\mathbf{I}_{Lf1e} &= j\frac{M}{\omega_0 L_{f1e}L_{f2e}}\mathbf{U}_{ab} = \frac{k\sqrt{L_1L_2}}{\omega_0 L_{f1e}L_{f2e}}U_{ab}\angle 0° \\
\mathbf{I}_{Lf2e} &= -j\frac{M}{\omega_0 L_{f1e}L_{f2e}}\mathbf{U}_{AB} = \frac{k\sqrt{L_1L_2}}{\omega_0 L_{f1e}L_{f2e}}U_{AB}\angle -90° \\
\mathbf{I}_{1e} &= -j\frac{1}{\omega_0 L_{f1e}}\mathbf{U}_{AB} = \frac{1}{\omega_0 L_{f1e}}U_{AB}\angle -90° \\
\mathbf{I}_{2e} &= j\frac{1}{\omega_0 L_{f2e}}\mathbf{U}_{ab} = \frac{1}{\omega_0 L_{f2e}}U_{ab}\angle 0°
\end{aligned} \tag{9}$$

The phase angles in (9) are concluded based on the fact that the voltage across the output rectifier depends on the current

through it, which means that $\mathbf{U}_{AB}$ and $\mathbf{I}_{Lf_{2e}}\mathbf{I}_{Lf_{2e}}$ are in phase. In addition, in order to focus on the main characteristics of the proposed topology, the operation conditions of continuous conduction through the rectifier are the major considerations of this paper. In this case, the accuracy of the equivalent circuit model in Fig. 8 is guaranteed. The advantages of the double-sided LCC compensated without magnetic integration can be easily derived from (9):

1) the current running through the transmitting coil $\mathbf{I}_{ie}$, which relates only to the inverter output voltage $\mathbf{U}_{AB}$, is independent of the load and the main coupling condition;
2) the output current $\mathbf{I}_{Lf2e}$ is proportional to $\mathbf{U}_{AB}$ when the pads are stationary, which simplifies the charging current regulation;
3) unity power factor can be realized on both sides of the circuit since the voltage and current extracting from the inverter and entering the rectifier are in phase, which minimizes the reactive power circulating in the main coils and the power supply.

However, these favorable features seem to be lost when the magnetic integration is implemented by comparing (7) with (9). To maintain these advantages, the integration-induced impacts should be discussed further.

B. Characteristic Analysis

It can be seen from (7) that all the currents are related to both the input and output voltage. The current through the power-transferring coils is considered first. Although the transmitting coil current is not affected by the main coupling *k* variation, the load voltage becomes a contributing factor, as it is superimposed on the transmitting coil through the integration-induced cross-side mutual inductance. The dominant phasors can be identified by the corresponding weight coefficients. The weight ratio of the voltage phasors imposed on $\mathbf{I}_{1e}$ and $\mathbf{I}_{2e}$ can be expressed as

$$m = \frac{M_{2f1}}{L_{f2e}} = \frac{M_{1f2}}{L_{f1e}} = \frac{M_{2f1}}{L_{f1}+M_{11}} = \frac{k_{12}}{\sqrt{L_{f1}\,/\,L_1}+k_{11}}. \tag{10}$$

Similarly, the weight ratio of the voltage phasors composing $\mathbf{I}_{Lf1e}$ and $\mathbf{I}_{Lf2e}$ is defined by

$$m_f = \frac{\Delta_2}{\Delta_1} = \frac{2\,L_{f2e}M_{1f2}}{L_{f1e}L_{f2e}+M_{1f2}M_{2f1}} = \frac{2m}{1+m^2}. \tag{11}$$

According to the previous simulation, k_{11} is several times larger than k_{12}. Meanwhile, L_{f1} is typically designed to be around the value of *M (*$0.1L_1$–$0.3L_1$*)*. As a result, *m* is actually a small fraction, as is m_f. In addition, as seen in wireless EV charging applications, the amplitudes of $\mathbf{U}_{\mathrm{AB}}$ and $\mathbf{U}_{ab}$ are comparable for most high-power-transferring operation conditions. Therefore, it can be concluded that the first items in (7) are the dominant phasors that play the decisive roles. Furthermore, the coefficients of the dominant phasors in (7) can be rewritten as

$$\Delta_1 = \frac{M}{\omega_0\left(L_{f1e}L_{f2e}-\frac{3-m^2}{1+m^2}M_{1f2}M_{2f1}\right)}$$

$$\Sigma_1 = \frac{L_{f1e}}{\omega_0 \mathrm{X}_i} = \frac{L_{f2e}}{\omega_0 \mathrm{X}_i} = \frac{1}{\omega_0\left(L_{f1e}-mM_{1f2}\right)}. \tag{12}$$

Compared to the coefficients presented in (9), it is evident that all the dominant vectors become slightly larger due to the extra couplings. However, the phase angle between the two superposing vectors must be explored before we can conclude that the amplitudes of the sum vector increase.

As mentioned earlier, $\mathbf{U}_{ab}$ and $\mathbf{I}_{Lf2e}$ are in phase in a unidirectional charging system. Assuming the phase angle of $\mathbf{U}_{ab}$ is φ while keeping $\mathbf{U}_{AB}$ as the reference, the current through the secondary compensated inductor $L_{f_{2e}}$ can be rewritten based on (7)

$$\begin{aligned}\mathbf{I}_{Lf2e} &= -j\Delta_1 U_{AB} + j\Delta_2 U_{ab}\left(\cos\left(\varphi\right)+j\sin\left(\varphi\right)\right)\\ &= -\sin\left(\varphi\right)\Delta_2 U_{ab} + j\left(\cos\left(\varphi\right)\Delta_2 U_{ab}-\Delta_1 U_{AB}\right)\end{aligned} \tag{13}$$

where U_{AB} and U_{ab} are the amplitudes. Consequently, the following equation can be obtained from (13):

$$\begin{aligned}\left|\mathbf{I}_{Lf2e}\right| &= \sqrt{\left(\mathrm{Re}\left(\mathbf{I}_{Lf2e}\right)\right)^2+\left(\mathrm{Im}\left(\mathbf{I}_{Lf2e}\right)\right)^2}\\ &= \Delta_1 U_{AB}\left|\sin\left(\varphi\right)\right|\end{aligned} \tag{14}$$

$$\begin{aligned}\tan\left(\varphi\right) &= \frac{\mathrm{Im}\left(\mathbf{I}_{Lf2e}\right)}{\mathrm{Re}\left(\mathbf{I}_{Lf2e}\right)} = \frac{\sin\left(\varphi\right)}{\cos\left(\varphi\right)}\\ &= \frac{\cos\left(\varphi\right)\Delta_2 U_{ab}-\Delta_1 U_{AB}}{-\sin\left(\varphi\right)\Delta_2 U_{ab}}.\end{aligned} \tag{15}$$

Further, (15) can easily be simplified as

$$\cos\left(\varphi\right) = \frac{\Delta_2}{\Delta_1}\frac{U_{ab}}{U_{AB}} = m_f G_V \tag{16}$$

where $G_V = U_{ab}\,/\,U_{AB}$ is the voltage gain. Since $\cos\left(\varphi\right) > 0$ and the dominant vector of $\mathbf{I}_{Lf2e}$ is located in the negative imaginary axis ($-j\Delta_1\mathbf{U}_{AB} = \Delta_1 U_{AB}\angle -90°$), φ is in the range of (–90°, 0°). It should be noted that in order to have (16) hold true, m_f should be smaller than the voltage gain to ensure the product is less than unity if $U_{ab} > U_{AB}$. In practice, an input threshold voltage can be found for a certain output voltage to get the power delivered to the secondary side, which forms the cutoff mode boundary. The maximum voltage gain of the cutoff boundary should be regarded as the upper limit of m_f. Then, we have

$$\sin\left(\varphi\right) = -\sqrt{1-\left(m_f G_V\right)^2} \tag{17}$$

$$\cot\left(\varphi\right) = -1\Big/\sqrt{\frac{1}{\left(m_f G_V\right)^2}-1}. \tag{18}$$

Likewise, if α is used to denote the phase angle of $\mathbf{I}_{Lf1e}$, it is easy to obtain

$$\mathbf{I}_{Lf1e} = -\sin\left(\varphi\right)\Delta_1 U_{ab} + j\left(\cos\left(\varphi\right)\Delta_1 U_{ab}-\Delta_2 U_{AB}\right) \tag{19}$$

$$\left|\mathbf{I}_{Lf1e}\right| = \Delta_1 U_{ab}\left|\sin\left(\varphi\right)\right| \,/\, \left|\cos\left(\alpha\right)\right| \tag{20}$$

$$\tan\left(\alpha\right) = \left(1\,/\,G_V^2-1\right)\cot\left(\varphi\right). \tag{21}$$

It can be observed from (16) that φ is roughly –90° if the parameter *m* is designed to be small when U_{AB} and U_{ab} are relatively close. In this circumstance, α is in the range of (–90°, 90°) and quite close to 0°, based on (21). Moreover, α will be negative if the condition $G_V < 1$ is satisfied, which means $\mathbf{I}_{Lf1e}$ lags behind $\mathbf{U}_{AB}$. It is preferred by the MOSFET-based inverter to realize a zero voltage switching (ZVS) operation. The value of the fundamental component of current at the switching moment is

$$\begin{aligned} I_{Lf1e,\mathrm{sw},1st} &= |\mathbf{I}_{Lf1e}| \cos(\omega t + \alpha)\big|_{\omega t=\pi/2} \\ &= |\mathbf{I}_{Lf1e}| \sin(-\alpha). \end{aligned} \tag{22}$$

Knowing the range of α and φ, we can obtain the following expression by substituting (20) and (21) into (22) successively:

$$\begin{aligned} I_{Lf1e,\mathrm{sw},1st} &= \Delta_1 U_{ab} \frac{|\sin(\varphi)|}{|\cos(\alpha)|} (-\sin(\alpha)) \\ &= \Delta_1 U_{ab} |\sin(\varphi)| (-\tan(\alpha)) \\ &= \Delta_1 U_{ab} |\sin(\varphi)| \left(1 - 1/G_V^2\right) \frac{\cos(\varphi)}{\sin(\varphi)} \\ &= \Delta_1 U_{ab} \left(1/G_V^2 - 1\right) \cos(\varphi). \end{aligned} \tag{23}$$

The switching current can be finally derived by substituting (16) into (23)

$$I_{Lf1e,\mathrm{sw},1st} = \Delta_2 \frac{U_{AB}^2 - U_{ab}^2}{U_{AB}}. \tag{24}$$

To achieve ZVS operation, the value of $I_{Lf1e,sw,1st}$ should be positive. Fortunately, it is possible to be realized during the CC charge stage when the battery voltage is low. The required charging current keeps decreasing in the succeeding constant voltage (CV) charge stage, while U_{AB} may be lower than U_{ab}. However, the ZVS condition can still be maintained for a while after α becomes positive, due to the contribution of the high-order harmonics [23]. The sum of the inverter high-order harmonic at the switching moment is expressed

$$I_{Lf1e,sw,high} = \frac{U_{AB}}{X_1} \sum_{k=1}^{\infty} \frac{1}{((2k+1)^2 - 1)} = \frac{U_{AB}}{4X_1}. \tag{25}$$

The actual inverter current value at the moment of switching is expressed as

$$\begin{aligned} I_{Lf1e,sw} &= I_{Lf1e,sw,1st} + I_{Lf1e,sw,high} \\ &= \left(\Delta_2 + \frac{1}{4X_1}\right) U_{AB} - \Delta_2 G_V U_{ab}. \end{aligned} \tag{26}$$

Therefore, for $\mathbf{I}_{Lf1e}$, though the magnetic integration increases the reactive input power, it is beneficial in forming the ZVS operation condition for the inverter. The amount of the increasing circulating energy is directly related to the angle φ according to (20) and (21).

Following the same route, the lengths and angles of the main coil current phasors can also be expressed analytically. Here, β and γ are used to represent the phase angles of $\mathbf{I}_{1e}$ and $\mathbf{I}_{2e}$, respectively. The following equations can be derived:

$$|\mathbf{I}_{1e}| = \Sigma_1 U_{AB} / |\sin(\beta) + \cot(\varphi)\cos(\beta)| \tag{27}$$

$$\tan(\beta) = (1/mm_f G_v^2 - 1)\cot(\varphi) \tag{28}$$

$$|\mathbf{I}_{2e}| = \Sigma_1 U_{ab} |\sin(\varphi)| / |\cos(\gamma)| \tag{29}$$

$$\tan(\gamma) = \left(m / m_f G_V^2 - 1\right)\cot(\varphi). \tag{30}$$

For comparison, (15) can be rewritten as

$$\tan(\varphi) = \left(1 / m_f^2 G_V^2 - 1\right)\cot(\varphi). \tag{31}$$

Again, *m* is a small fraction. Hence, m^2 is negligible, and $m_f \approx 2m$ from (11). By comparing (28) to (31) and (30) to (21), respectively, it can be inferred that $\beta \approx \varphi \approx$ –90° and $\gamma \approx \alpha \approx 0°$ when G_V is around unity.

Finally and more importantly, the transferring power can be calculated by

$$P_{in} = \mathrm{Re}\left(\frac{\mathbf{U}_{AB}\mathbf{I}_{\mathbf{f1e}}^*}{2}\right) = -\frac{1}{2}\sin(\varphi)\Delta_1 U_{ab} U_{AB}. \tag{32}$$

Substituting (12) and (17) into (32), we have

$$P_{in} = \frac{\sqrt{1 - \left(m_f \frac{U_{ab}}{U_{AB}}\right)^2}\sqrt{L_1 L_2}}{2\omega_0 \left(L_{f1e}L_{f2e} - \frac{3-m^2}{1+m^2} M_{1f2}M_{2f1}\right)} k U_{AB} U_{ab}. \tag{33}$$

In brief, there are mainly two impacts caused by the compensated inductor integration. First, although the extra same-side couplings do not affect the construction of LCL-T resonant converter on both sides at all. The parameter design becomes harder since the inductors are all coupled. Second, the extra cross-side couplings slightly decrease the system power factor, which may reduce the efficiency. However, the negative effect can be minimized by having the parameter *m* expressed in (10) as small as possible. Fortunately, *m* is limited naturally by the large clearance between the EV charging pads. Therefore, compared to the cumbersome nonintegrated topology, the extra effort on the integrated coupler design is worthy.

C. Conduction Losses Estimation

To calculate the output power, the losses should be estimated. There are both conduction losses and magnetic losses in the WPT system. The conduction losses in the compensation components can be calculated according to the parasitic resistance. First, the parasitic resistance of the capacitor is calculated as

$$R_C = \frac{D_F}{\omega C} = \frac{D_F}{2\pi f_{sw} \cdot C} \tag{34}$$

where D_F is the dissipation factor of the selected capacitor. To achieve low loss and low temperature rise in the compensation capacitors, a low dissipation at the operation frequency factor is required.

Second, litz wire is usually used to construct the coils in order to reduce the conduction loss at high frequency. Losses in litz wires consist of resistive loss and eddy-current loss, which can be further classified into skin effect and proximity effect. By selecting the wire diameter smaller than the skin depth at the aimed frequency, the skin-effect loss can be minimized. However, the bundle-level proximity loss should be taken into account [24]. The ac resistance of the coils in the WPT system

TABLE I
WIRELESS EV CHARGER SPECIFICATIONS

Spec/Parameters	Value
Input voltage	$<=450$ V
Output voltage	300–450 V
Nominal gap between pads	150 mm
X-misalignment (door to door) tolerance	300 mm
Y-misalignment (front to rear) tolerance	125 mm
Switching frequency	95 kHz
Rated power	6 kW
Power-transferring coupling coefficient k	0.14–0.30
Transmitting/pickup coil inductance L_1, L_2	260 μH
Equivalent compensated inductance L_{f1e}, L_{f2e}	60 μH
Paralleled compensated capacitance C_{f1}, C_{f2}	77.9 nF
Series compensated capacitance C_1, C_2	12.5 nF
Magnetic integration impact factor m	<0.15
Pads' physical size	600 mm $\times$ 600 mm
Litz-wire	AWG38 $\times$ 800

is, therefore, estimated as

$$R_{L,ac} = k_{pe} \cdot R_{L,dc} = k_{pe} \cdot \rho l \,/\, N \tag{35}$$

where ρ is the resistivity of the selected litz wire, l is the length of the wire, N is the number of strands, and k_{pe} is the coefficient caused by the bundle-level proximity effect, which is found to be 1.5–2.5 referring to [24].

Knowing the parasitic parameters, the conduction losses are therefore shown as

$$\begin{aligned} P_{lc} = {} & I^2_{Lf1e,RMS} R_{Lf1,ac} + I^2_{Cf1e,RMS} R_{Cf1} \\ & + I^2_{1e,RMS} \left(R_{C1} + R_{L1,ac}\right) \\ & + I^2_{Lf2e,RMS} R_{Lf2,ac} + I^2_{Cf2e,RMS} R_{Cf2} \\ & + I^2_{2e,RMS} \left(R_{C2} + R_{L2,ac}\right). \end{aligned} \tag{36}$$

The RMS current through the components can be calculated based on the results of (14), (20), (27), and (29). Besides, the magnetic losses P_{lm} should be estimated according to the FEM simulation results due to the unconventional flux distribution between the pads, which is out of the scope of this paper. Therefore, the transferred power can be estimated by $P_o = P_{in} - P_{lc} - P_{lm}$.

IV. EXPERIMENTAL VALIDATION

To demonstrate the proposed topology and the above analysis, a prototype of a WPT charging system that features the magnetic integrated DD pads compensated by double-sided LCC networks has been built. The specifications of the prototype are given in Table I.

The finished pads are shown in Fig. 9. The size of the compensated coil is designed to be 200 mm $\times$ 200 mm according to the FEA simulation results. Although the compensated capacitors in Fig. 9 are located outside of the pad, they actually can be lumped together if a custom-built coil holder is adopted. Ferrites are usually arranged into several discrete rows with a length smaller than the pad. Further compensation integration can be accomplished by making good use of the spare space left in the ferrite layer to place the compensated capacitors. In

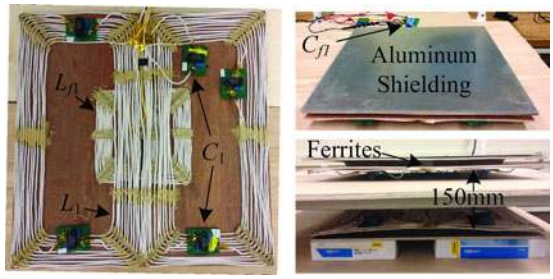

Fig. 9. Constructed compensation integrated DD pads.

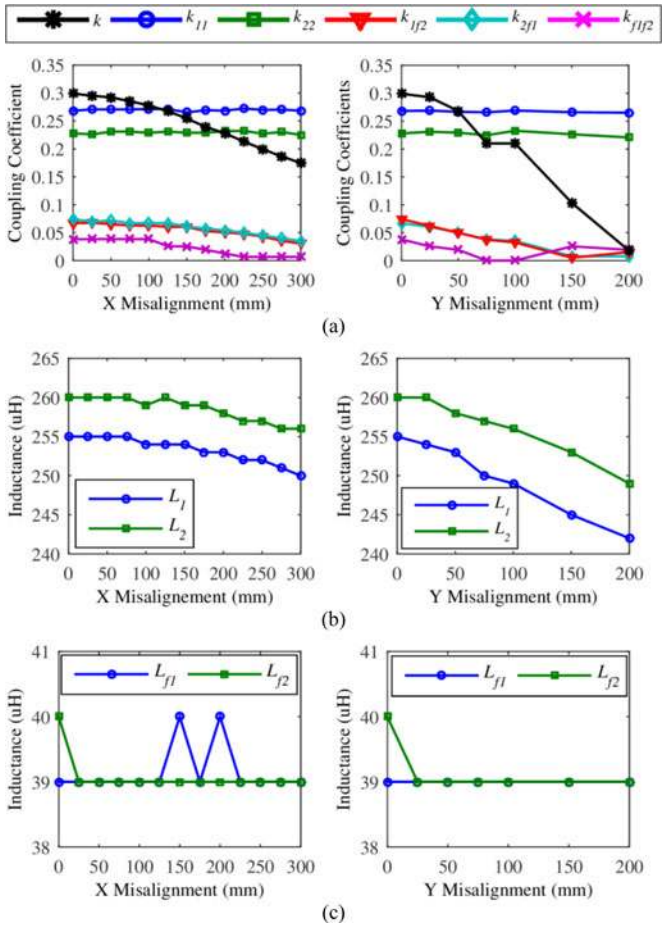

Fig. 10. Parameter variations due to misalignments. (a) Coupling coefficients. (b) Main coil inductances. (c) Compensated coil inductances.

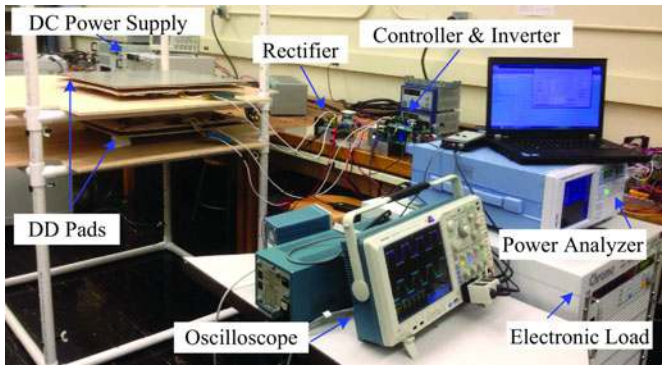

Fig. 11. Physical setup of the tested prototype.

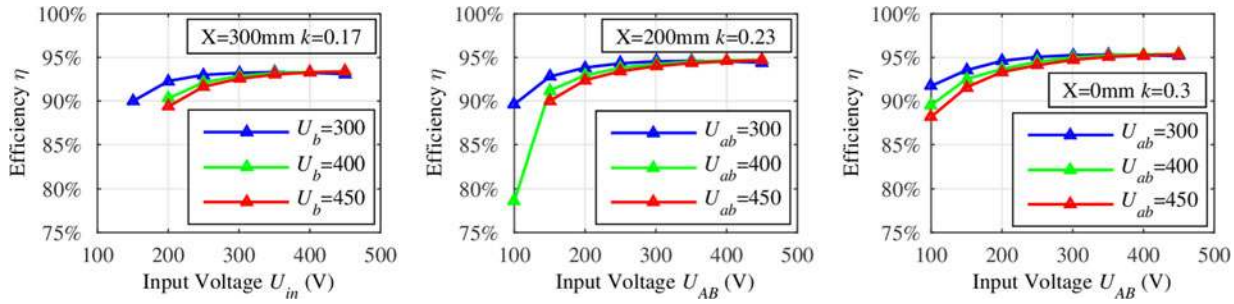

Fig. 12. Experimental efficiencies of the system when output voltages are 300, 400, and 450 V at different x-direction misalignments. (a) x-misalignments = 300 mm. (b) x-misalignments = 200 mm. (c) x-misalignments = 0 mm.

this case, the bulky LCC compensation network can be lumped together with the main coil and thus appears as a whole pad. Compared to the nonintegrated double-side LCC compensated DD pads presented in [8], about 0.4 L volume is saved for the separated air-core-compensated inductors. In addition, the 0.13 L paralleled compensated capacitors can also be embedded in the ferrite layer. Besides, the spread planar-type compensated inductors are better for the natural cooling.

The variations of the coupling coefficients and the inductances due to horizontal misalignments are given in Fig. 10 according to experimental measurements. The results show that 1) the extra same-side couplings do not vary with misalignments because of their tight attachment, while the extra cross-side couplings drop visibly, which matches the simulated results in Section II; 2) the extra same-side couplings are four times larger than the extra cross-side couplings; 3) because the same-side coils could not be exactly distributed in different layers without a holder, the measured same-side coupling coefficients are larger than the simulated results; 4) k_{f1f2} is the smallest one, as we expected; 5) the compensated coil inductance can be regarded as constant, due to the relatively large gap/size ratio; 6) the inductance variation of the main coils is very close to the simulation results; and 7) the inductance and the same-side couplings of the transmitting side and pickup side are not exactly identical (around 2% difference) due to the fabrication imperfection. Finally, the integration impact factor $m = 0.11$ can be calculated based on the experimental results, which is a small fraction, as we estimated.

The experimental setup is shown in Fig. 11. As can be seen, the constructed pads were placed in the fixture. The vertical gap and the horizontal misalignments can be adjusted as needed. The dc power from the power supply is converted to high-frequency ac power and injected into the bottom transmitting pad. The induced high-frequency ac power in the upper pickup pad is rectified and filtered. An electronic load is used to emulate the CV characteristic of the battery. A power analyzer WT1600 from Yokogawa is connected to the system to calculate the efficiency by measuring the output power from the dc source and the input power to the electronic load. Fig. 12 shows the efficiency curves from a dc power source to the battery load for the proposed WPT system under different conditions. From Fig. 12(a), we find that the efficiency is higher than 90% even at a large x-direction misaligned condition. The maximum measured efficiency is 95.36% when $U_{in} = 450$ V, $U_b = 450$ V,

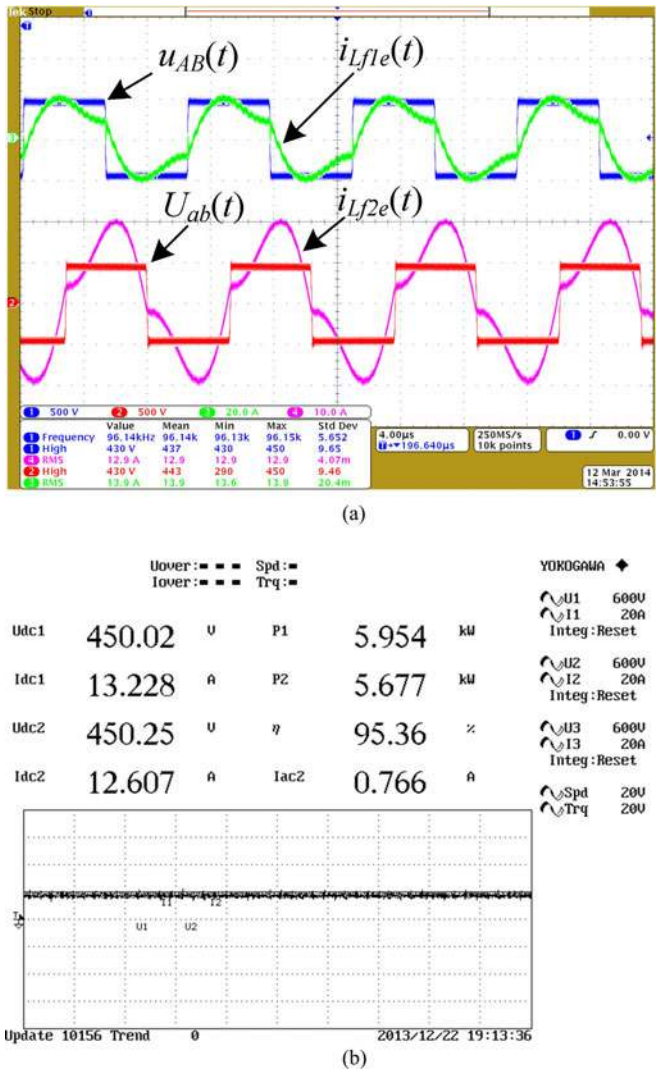

Fig. 13. Peak efficiency operation point at X-misalignment = 0 mm, $U_{in} = 450$ V, $U_b = 450$ V, $P_o = 5.6$ kW. (a) Waveforms of primary inverter output and secondary rectifier input. (b) Capture of the power analyzer.

and $k = 0.3$ as shown in Fig. 12(c). The primary-side waveforms and secondary-side waveforms are shown in Fig. 13 when the system operates at the peak efficiency steady state, delivering 5.6 kW to the load. It can be seen that the inverter output current $i_{Lf1e}(t)$ lags slightly behind the inverter voltage; hence, the soft-switching operation is realized. In addition, the phase

angle of $\mathbf{U}_{\rm ab}$ and $\mathbf{I}_{Lf2e}$ is about –80° in Fig. 12(a), since the rectifier is conducted continuously and $U_{AB} = U_{ab}$, which can be calculated using (16).

V. Conclusion

A magnetic-integrated bipolar coupler has been proposed in order to improve the compactness of the double-side LCC compensated WPT topology. The compensation inductors are flattened to be smaller DD coils and inserted into the traditional DD coupler. The proposed structure spares the space and magnetic cores outside of the coupler, which are normally needed for the compensation inductors. The characteristics of the proposed coupler, especially the extra integration-induced couplings, are studied by FEA. The feasibility of the proposed topology is investigated through the equivalent circuit modeling and analysis. It is found that the unwanted impacts of the magnetic integration can be minimized by reducing the extra cross-side couplings in the coupler design. The proposed structure and corresponding analysis are validated through experiments on a prototype.

References

[1] S. Y. Choi, J. Huh, W. Y. Lee, and C. T. Rim, "Asymmetric coil sets for wireless stationary EV chargers with large lateral tolerance by dominant field analysis," *IEEE Trans. Power Electron.*, vol. 29, no. 12, pp. 6406–6420, Dec. 2014.

[2] Q. Zhu, L. Wang, and C. Liao, "Compensate capacitor optimization for kilowatt-level magnetically resonant wireless charging system," *IEEE Trans. Ind. Electron.*, vol. 61, no. 12, pp. 6758–6768, Dec. 2014.

[3] C. Huang, J. E. James, and G. A. Covic, "Design considerations for variable coupling lumped coil systems," *IEEE Trans. Power Electron.*, vol. 30, no. 2, pp. 680–689, Feb. 2015.

[4] N. Puqi, J. M. Miller, O. C. Onar, and C. P. White, "A compact wireless charging system for electric vehicles," in *Proc. IEEE Energy Convers. Congr. Expo.*, 2013, pp. 3629–3634.

[5] S. Li and C. Mi, "Wireless power transfer for electric vehicle applications," *IEEE J. Emerg. Sel. Topics Power Electron.*, vol. 3, no. 1, pp. 4–17, Mar. 2015.

[6] H. H. Wu, A. Gilchrist, K. D. Sealy, and D. Bronson, "A high efficiency 5 kW inductive charger for EVs using dual side control," *IEEE Trans. Ind. Informat.*, vol. 8, no. 3, pp. 585–595, Aug. 2012.

[7] M. Budhia, G. A. Covic, and J. T. Boys, "Design and optimization of circular magnetic structures for lumped inductive power transfer systems," *IEEE Trans. Power Electron.*, vol. 26, no. 11, pp. 3096–3108, Nov. 2011.

[8] D. Kurschner, C. Rathge, and U. Jumar, "Design methodology for high efficient inductive power transfer systems with high coil positioning flexibility," *IEEE Trans. Ind. Electron.*, vol. 60, no. 1, pp. 372–381, Jan. 2013.

[9] M. Budhia, G. Covic, and J. Boys, "A new IPT magnetic coupler for electric vehicle charging systems," in *Proc. IEEE 36th Annu. Conf. Ind. Electron. Soc.*, 2010, pp. 2487–2492.

[10] Y. Nagatsuka, N. Ehara, Y. Kaneko, S. Abe, and T. Yasuda, "Compact contactless power transfer system for electric vehicles," in *Proc. Int. Power Electron. Conf.*, 2010, pp. 807–813.

[11] M. Budhia, J. T. Boys, G. A. Covic, and H. Chang-Yu, "Development of a single-sided flux magnetic coupler for electric vehicle IPT charging systems," *IEEE Trans. Ind. Electron.*, vol. 60, no. 1, pp. 318–328, Jan. 2013.

[12] W. Zhang, S.-C. Wong, C. K. Tse, and Q. Chen, "Design for efficiency optimization and voltage controllability of series-series compensated inductive power transfer systems," *IEEE Trans. Power Electron.*, vol. 29, no. 1, pp. 191–200, Jan. 2014.

[13] W. Zhang, S.-C. Wong, C. K. Tse, and Q. Chen, "Analysis and comparison of secondary series- and parallel-compensated inductive power transfer systems operating for optimal efficiency and load-independent voltage-transfer ratio," *IEEE Trans. Power Electron.*, vol. 29, no. 6, pp. 2979–2990, Jun. 2014.

[14] C. Wang, O. H. Stielau, and G. A. Covic, "Design considerations for a contactless electric vehicle battery charger," *IEEE Trans. Ind. Electron.*, vol. 52, no. 5, pp. 1308–1314, Oct. 2005.

[15] A. Khaligh and S. Dusmez, "Comprehensive topological analysis of conductive and inductive charging solutions for plug-in electric vehicles," *IEEE Trans. Veh. Technol.*, vol. 61, no. 8, pp. 3475–3489, Oct. 2012.

[16] C. Shin-Young, L. Il-Oun, M. SangCheol, M. Gun-Woo, K. Bong-Chul, and K. Ki Young, "Series-series compensated wireless power transfer at two different resonant frequencies," in *Proc. IEEE Energy Convers. Congr. Expo. Asia*, 2013, pp. 1052–1058.

[17] C. Wang, G. A. Covic, and O. H. Stielau, "Investigating an LCL load resonant inverter for inductive power transfer applications," *IEEE Trans. Power Electron.*, vol. 19, no. 4, pp. 995–1002, Jul. 2004.

[18] A. P. Hu, *Wireless/Contactless Power Supply: Inductively Coupled Resonant Converter Solutions*. Saarbrücken, Germany: VDM Publishing, 2009, pp. 139–141.

[19] M. Borage, S. Tiwari, and S. Kotaiah, "Analysis and design of an LCL-T resonant converter as a constant-current power supply," *IEEE Trans. Ind. Electron.*, vol. 52, no. 6, pp. 1547–1554, Dec. 2005.

[20] N. A. Keeling, G. A. Covic, and J. T. Boys, "A unity-power-factor IPT pickup for high-power applications," *IEEE Trans. Ind. Electron.*, vol. 57, no. 2, pp. 744–751, Feb. 2010.

[21] N. Trong-Duy, S. Li, W. Li, and C. C. Mi, "Feasibility study on bipolar pads for efficient wireless power chargers," in *Proc. IEEE Appl. Power Electron. Conf. Expo.*, 2014, pp. 1676–1682.

[22] A. Kurs, A. Karalis, R. Moffatt, J. D. Joannopoulos, P. Fisher, and M. Soljačić, "Wireless power transfer via strongly coupled magnetic resonances," *Science*, vol. 317, no. 5834, pp. 83–86, Jun. 2007.

[23] Z. Pantic, S. Bai, and S. Lukic, "ZCS LCC-compensated resonant inverter for inductive-power-transfer application," *IEEE Trans. Ind. Electron.*, vol. 58, no. 8, pp. 3500–3510, Aug. 2011.

[24] C. R. Sullivan and R. Y. Zhang, "Analytical model for effects of twisting on litz-wire losses," in *Proc. IEEE 15th Workshop Control Model. Power Electron.*, 2014, pp. 1–10.

Junjun Deng (S'13–M'14) received the B.S. and M.S. degrees in electrical engineering from Northwestern Polytechnical University, Xi'an, China, in 2008 and 2011, respectively. He is currently working toward the Ph.D. degree in electrical engineering from the Northwestern Polytechnical University.

From 2011 to 2013, he was a joint Ph.D. student founded by the China Scholarship Council with the University of Michigan, Dearborn, MI, USA. From 2013 to 2014, he was a Research Assistant with the Department of Electrical and Computer Engineer, University of Michigan, Dearborn. His research interests include wireless power transfer, resonant power conversion, and high-performance battery chargers for electric vehicles.

Weihan Li (S'13) reveived the B.S. degree in automotive engineering from the Hefei University of Technology, Hefei, China, in 2010, where he is currently working toward the Ph.D. degree in automotive engineering from Hefei University of Technology.

From September 2012 to August 2014, He was a joint Ph.D. student founded by China Scholarship Council with GATE Center for Electric Drive Transportation, Department of Electrical and Computer Engineering, University of Michigan, Dearborn, where he is involved in the modeling and design of wireless charger for electric vehicles/plug-in hybrid electric vehicles (EVs/PHEVs). His research interests include wireless power transfer, EV/PHEV system, renewable energy, and power electronics.

Trong Duy Nguyen was born in Binh Dinh, Vietnam. He received the B.Eng. and M.Eng. degrees from the Ho Chi Minh City University of Technology, Ho Chi Minh City, Vietnam, and the Ph.D. degree from the Nanyang Technological University, Singapore.

His current research interests include electrical machine design and drives, electromagnetics, and electrical energy conversion systems.

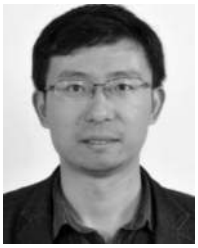

Siqi Li (M'13) received the B.S. and Ph.D. degrees in electrical engineering from Tsinghua University, Beijing, China, in 2004 and 2010, respectively.

He was a Postdoctoral Fellow with the University of Michigan, Dearborn, MI, USA, from 2011 to 2013. In 2013, he joined the Faculty of Electric Power Engineering, Kunming University of Science and Technology, Kunming, China, where he is currently an Associate Professor with the Department of Electrical Engineering. He is also the director of the Advanced Power Electronics and New Energy Laboratory. His research interest focuses on battery management system and high-performance wired and wireless battery chargers for electric vehicles.

Chunting Chris Mi (S'00–A'01–M'01–SM'03–F'12) received the B.S.E.E. and M.S.E.E. degrees in electrical engineering from Northwestern Polytechnical University, Xi'an, China, and the Ph.D. degree in electrical engineering from the University of Toronto, Toronto, ON, Canada.

He is currently a Professor of electrical and computer engineering and the Director of the Department of Energy-funded Graduate Automotive Technology Education Center for Electric Drive Transportation, University of Michigan, Dearborn, Michigan, MI, USA. Prior to joining the University of Michigan, Dearborn, in 2001, he was with General Electric Company, Peterborough, ON, Canada. He was the President and the Chief Technical Officer of 1Power Solutions, Inc., from 2008 to 2011. He is the Co-Founder of Gannon Motors and Controls LLC and Mia Motors, Inc. His research interests include electric drives, power electronics, electric machines, renewable energy systems, and electrical and hybrid vehicles. He has conducted extensive research and has published more than 100 journal papers. He has taught tutorials and seminars on the subject of HEVs/PHEVs for the Society of Automotive Engineers (SAE), the IEEE, workshops sponsored by the National Science Foundation (NSF), and the National Society of Professional Engineers. He has delivered courses to major automotive OEMs and suppliers, including GM, Ford, Chrysler, Honda, Hyundai, Tyco Electronics, A&D Technology, Johnson Controls, Quantum Technology, Delphi, and the European Ph.D School. He has offered tutorials in many countries, including the U.S., China, Korea, Singapore, Italy, France, and Mexico. He has published more than 100 articles and delivered 30 invited talks and keynote speeches. He has also served as a panelist in major IEEE and SAE conferences.

Dr. Mi is the recipient of "Distinguished Teaching Award" and "Distinguished Research Award" of University of Michigan Dearborn. He is a recipient of the 2007 IEEE Region 4 "Outstanding Engineer Award," "IEEE Southeastern Michigan Section Outstanding Professional Award," and the "SAE Environmental Excellence in Transportation (E2T).